ERRATA

This article was originally published in [J. Mater. Res. 19, 707 (2004)] and was incorrectly printed. The correct version appears below.

Erratum: "A comparison of pseudomorphic bcc phase stability in Zr/Nb and Ti/Nb thin film multilayers" [J. Mater. Res. 19, 707 (2004]

G.B. Thompson,[a] R. Banerjee, and S.A. Dregia
Materials Science and Engineering Department, The Ohio State University, Columbus, Ohio 43210
M.K. Miller
Metals and Ceramic Division, Oak Ridge National Laboratory, Oak Ridge, Tennessee 37831
H.L. Fraser
Materials Science and Engineering Department, The Ohio State University, Columbus, Ohio 43210

(Received 9 May 2003; accepted 8 October 2003)

A series of Nb-rich Zr/Nb and Ti/Nb multilayers were sputter deposited. Upon a reduction in thickness, a pseudomorphic bcc phase was stabilized in the Zr and Ti layers. X-ray and electron diffraction techniques were used to confirm these phase transformations. The change in phase stability was modeled by the competition between volumetric and interfacial components of the total free energy of a unit bilayer representing the multilayer. An outcome of this model is the ability to plot phase stability diagrams for multilayers, referred to as biphase diagrams, as a function of bilayer thickness and volume fraction. A comparison of the phase stability boundary between hcp/bcc and bcc/bcc for these two systems has shown that the bcc Ti's pseudomorphic phase stabilization is maintained for a much larger layer thickness as compared to Zr. Atom probe compositional profiles of the Ti/Nb multilayers have indicated that the Nb layers interdiffused into the Ti layers thus helping to facilitate the bcc Ti phase stability in the Ti/Nb multilayers.

I. INTRODUCTION

When thin films grow epitaxially on a substrate, crystallographic phases that are not observed in the standard state of 1 atm and 298 K may result in the film during the early stages of growth. This is referred to as pseudomorphic growth. Formation of pseudomorphic phases has been reported for single thin films on substrates[1–3] as well as in individual layers in multilayered thin films.[4–6] Recently, Dregia et al.[7] have reported a model, based on classical thermodynamics, that can predict phase stability of pseudomorphic phases in thin film multilayers. In this model, pseudomorphic phases are stabilized by the competition between the volumetric and interfacial components of the total free energy. At a critical transition thickness, the decrease in the interfacial free energy component can more than compensate for the increase in the volumetric free energy component, and a pseudomorphic phase within one (or both) layers of the multilayer can be stabilized. Dregia et al.[7] have modeled this change in phase stability in multilayers by considering a unit bilayer representing the A/B multilayered stack. This unit bilayer consists of a layer of A, a layer of B, and two A/B interfaces. The two independent degrees of freedom in the unit bilayer are the bilayer thickness, λ, which is equivalent to the layer thickness of A plus B, and the volume fraction, f_i, where i is either A or B. The free energy difference between the pseudomorphic and bulk equilibrium states of the multilayer is then given as

$$\Delta G = 2\Delta\gamma A + [\Delta G_A f_A + \Delta G_B (1 - f_A)]\lambda A + E_s \lambda A \quad , \tag{1}$$

where $\Delta\gamma$ is the interfacial free energy difference between pseudomorphic and bulk equilibrium states of the bilayer, ΔG_i is the allotropic volumetric free energy difference between the pseudomorphic and bulk equilibrium states of layer i, A is the interfacial area, E_s is the strain energy contribution, and λ and f_i are as defined above. Strain energy can be significant for some materials in stabilizing the pseudomorphic phase. To maintain

[a]Present address: Department of Metallurgical and Materials Engineering, University of Alabama, Tuscaloosa, AL 35487.

DOI: 10.1557/JMR2004.0091

the simplicity of this model's description in the subsequent sections of this paper, it will be assumed that all terms that scale with volume, such as strain, are contained in the ΔG_i terms, and all terms that scale with area are contained in the $\Delta\gamma$ term. It has been shown elsewhere that when necessary, the strain energy, E_s, can be treated and calculated as an individual component in the description of Eq. (1).[6,8] In the thermodynamic framework of Eq. (1), the ΔG_i term was converted from an energy per mole value, common in the literature, to an energy per volume using an average atomic density of the pseudomorphic and bulk equilibrium phases for each of the materials. Table I is a tabulation of the ΔG_is used in this paper. A convenient representation of phase stability as a function of the two independent degrees of freedom is a plot of $1/\lambda$ verses f_i. This has been referred to as a *biphase diagram*.[7] For a single transformation in Eq. (1), the slope on the biphase stability diagram[7] that separates the bulk equilibrium and pseudomorphic phase stability regions is given as

$$\text{slope} = \Delta G_i / 2\Delta\gamma \quad . \tag{2}$$

By experimentally determining the slope of this phase stability boundary and using computed values for ΔG_i, the interfacial free-energy change, $\Delta\gamma$, can be estimated from Eq. (2). If the boundary of this slope is linear, it implies that there are negligible coherency strains[7] and the free energies are independent of volume fraction and bilayer spacing. In contrast, if the boundary is curved, coherency strains are not negligible as these strains will scale with volume fraction, and the thermodynamic equation given in Eq. (1) needs to be properly extended to account explicitly for E_s in measuring the interfacial energy.[6,8] Thus, the location of the data points on the biphase diagram can be used to determine the extent of coherency strains in the system.

As outlined in the thermodynamic framework of a unit bilayer, and experimentally confirmed, the order of layering deposition was independent of the phase stability of the multilayer; that is, Zr (or Ti) initially grown on the Nb layer or Nb initially grown on a Zr (or Ti) layer. It is interesting to note that the thermodynamics require two interfaces to stabilize the pseudomorph. It is possible that a layer can initially deposit with its equilibrium phase while in contact with one interface but then undergo a Martensitic type of diffusionless transformation under the growth front once the second layer (second interface) has been deposited on top of it. The thermodynamics only account for the initial and final energy states of the system and not the path in which the system achieves equilibrium.

TABLE I. The calculation of the reduction in the interfacial free energy, $\Delta\gamma$, estimated using the van der Merwe interfacial free energy model.

Multilayer	$\Delta\gamma$ (mJ/m^2) calculated	$\Delta\gamma$ (mJ/m^2) experimental	$\Delta G_{\text{bcc-hcp}}$ (J/m^3) [Ref.]
Zr/Nb	−240	−250	$\Delta G_{\text{Zr}} = 3.6 \times 10^8$ [9]
Ti/Nb	−280	−583	$\Delta G_{\text{Ti}} = 3.5 \times 10^8$ [10]
Ti–20 Nb/Nb	···	−283	$\Delta G_{\text{Ti-20Nb}} = 1.7 \times 10^8$ [10]

The experimentally estimated interfacial free energy values were determined from the slope of the biphase stability diagram for the Zr/Nb and Ti/Nb multilayers. The strain-free ΔG_i values are also tabulated.

The factors that influence the formation of pseudomorphic body-centered-cubic (bcc) Zr in Zr/Nb multilayers have been discussed elsewhere.[8] The change in phase stability of Zr from hexagonal-close-packed (hcp) to bcc, established by electron diffraction in the previous paper,[8] has been confirmed in this report by the use of transmission x-ray diffraction (XRD). The use of electron diffraction as a legitimate technique in phase identification of pseudomorphic phases in multilayers has been debated.[11,12] The transmission XRD results validate the use of plan-view electron diffraction for phase identification in the systems discussed in this paper.

Zheng et al.,[13] while investigating the superconducting properties of Ti/Nb multilayers, have reported phase stability changes in the Ti layer. However, their results concerning the phase stability in the Ti layers are rather confused.[13] Additionally, details of the layer thickness and volume fractions at which changes in phase stability occur were not listed in their work. In this paper, the stabilization of bcc Ti in Ti/Nb has been systematically presented and compared to that of bcc Zr in Zr/Nb multilayers. Note that both Zr and Ti bulk alloys undergo an allotropic phase transformation from α hcp to β bcc prior to the liquid phase with increasing temperature.[14]

II. EXPERIMENTAL

A series of Zr/Nb and Ti/Nb multilayers with varying volume fractions and bilayer thicknesses were sputter-deposited on oxidized Si substrates. The base pressure of the deposition chamber prior to sputtering was approximately 4×10^{-9} Torr. Ultra-high-purity Ar was used as the working gas at a pressure of 2–3 mTorr. Commercial purity elemental sputtering targets were used for depositing the multilayers. The targets were power regulated at 100 W during sputtering with deposition rates of approximately 0.1 nm/s. Each multilayer was deposited with 40 layer pairs by rotating the substrate between the two respective targets.

The phases in the multilayers were characterized using x-ray and electron diffraction techniques. X-ray diffraction was performed in both the reflection and transmission geometries. Reflection x-ray diffraction (RXRD) was conducted on a Scintag (Cypertino, CA) XDS 2000 diffractometer operating at 45 keV, 20 mA Cu Kα radiation (0.154 nm). The scans were continuous at a rate

of 0.5°/min with a chopper increment of 0.03°. Satellite reflections from the periodic layering of the multilayer's chemical modulations in the RXRD geometry were used to verify the bilayer spacing, λ, for each multilayer.

Transmission x-ray diffraction (TXRD) was performed at the Advanced Photon Source located at Argonne National Laboratory. TXRD experiments were conducted at an energy of 15.05 keV (0.0821 nm) in University-National Laboratory-Industry Collaborative Access Team's 33BM Beamline. The synchrotron energy allowed x-ray penetration through the Si wafer and multilayered film, thus allowing the specimens to be characterized in the as-deposited state on the substrate. Transmission eelectron microscopy (TEM) phase identification was performed in the plan-view geometry. TEM was conducted on a FEI (Willsboro, PA) Philips CM 200 microscope operating at 200 keV. The TEM plan-view specimens were prepared by ultrasonically drilling 3-mm disks from the Si wafer using a SiC slurry. The disks were then mechanically ground from the Si side to a thickness of approximately 100 μm with an additional dimple grinding at the center of the disks to approximately 15 μm in thickness. In the final preparation step, the disks were Ar^+ ion-milled at 9° on the dimpled wafer side until electron transparent. The chemical composition of the films was verified using energy dispersive spectroscopy (EDS) on a FEI XL 30 scanning electron microscope.

Atom probe tomography (APT), due to its subnanometer spatial resolution, was used to characterize the chemical composition of the multilayers. The atom probe experiments were performed in an energy-compensated optical-position-sensitive atom probe unit maintained at Oak Ridge National Laboratory through the SHaRE user program. The multilayers were prepared in a similar manner described by Larson et al.[15] and have been reported elsewhere[16] in detail by the authors. In general, the multilayered film is deposited onto a prefabricated Si wafer that has been reactively ion etched into a series of 5 × 5 × 80 μm posts. A single post with a multilayer film grown on its surface is then attached to a handling needle. The needle with post is then loaded into a FEI db-235 and annularly ion-milled using a focused ion beam (FIB) into the appropriate hemispherical shape tip required to field evaporate atoms in the atom probe. The authors have in situ deposited a cap of Pt on the surface of the film in the FIB prior to milling to reduce the implantation of Ga into the film which can generate milling artifacts in the specimen.[16]

III. RESULTS

Each multilayer deposited in this study exhibited polycrystalline grain growth with grain sizes ranging from 15 to 50 nm. Each film grew with a preferred growth texture

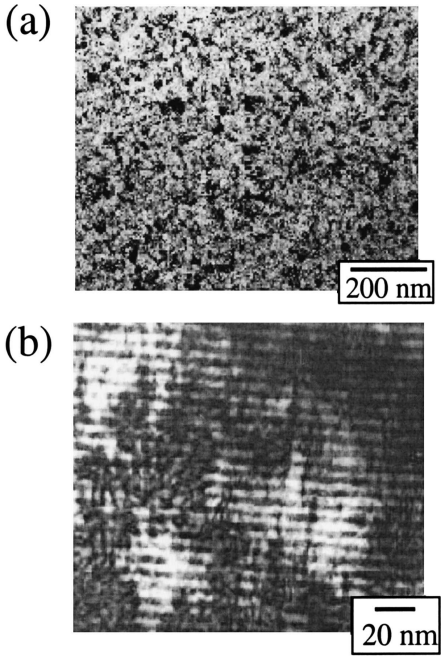

FIG. 1. (a) A representative plan-view TEM bright-field image of the multilayers reported in this paper. This specimen is of a Ti/Nb multilayer. Note the polycrystalline morphology with grains of 15–50 nm. (b) A representative cross-sectional TEM bright-field image of the multilayers reported. This sample is of a Ti/Nb multilayer. The multilayers have uniform lamellar interfaces with a columnar grain morphology.

such that the closest packed planes, for example {0002} hcp and {011} bcc, were oriented parallel to the substrate surface. The oxide surface of the substrate and the ambient growth temperature prevented any epitaxial orientation relationship between the substrate and film. A representative bright-field plan-view geometry TEM image of the multilayers is shown in Fig. 1(a). A corresponding cross-sectional TEM image of the multilayers prepared by focused ion beam milling is shown in Fig. 1(b). It is clear from Fig. 1(b) that the multilayers have morphologically uniform interfaces between the constituent layers.

The experimentally determined biphase stability diagram for the Zr/Nb multilayers is plotted in Fig. 2(a).[8] The change in phase stability in the Zr layers from hcp to bcc can be seen in Figs. 2(b) and 2(c). In Fig. 2(b), the TXRD pattern exhibits both the $\{10\bar{1}0\}$ peak of hcp Zr and the {110} peak of bcc Nb. This specimen is labeled #1 on Fig. 2(a). Upon a reduction in the bilayer thickness [specimen #2 on Fig. 2(a)], the Zr layer undergoes a change in phase stability from hcp to bcc as evident from the loss of the $\{10\bar{1}0\}$ peak of hcp Zr in the TXRD pattern shown in Fig. 2(c). The change in phase stability is referenced to the bulk state to be consistent within the thermodynamic framework description given above. The TXRD results confirm the previously reported hcp to bcc phase stability change in Zr in Zr/Nb multilayers by plan-view TEM diffraction.[8] In the previous work,[8]

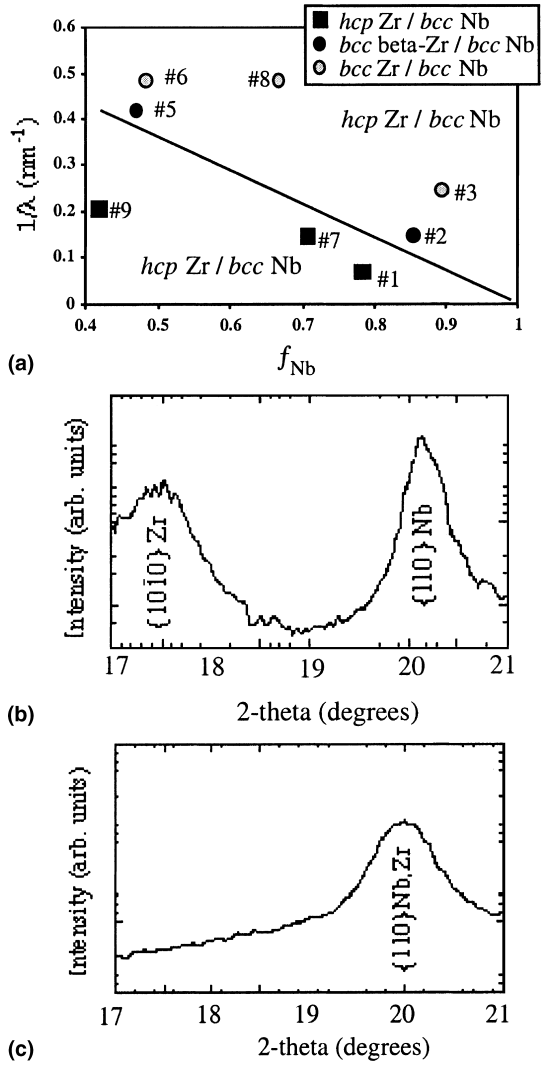

FIG. 2. (a) Biphase stability diagram[8] for the Zr/Nb multilayers as a function of volume fraction and bilayer thickness. (b) Transmission XRD pattern taken in the as-deposited state of a hcp Zr/bcc Nb #1 multilayer. (c) Transmission XRD taken in the as-deposited state of the bcc Zr/bcc Nb #2 multilayer.

the authors have shown that the {110} intensity ring in the plan-view TEM pattern is asymmetric. Deconvolution has indicated that the Zr layer has a lattice parameter near that of its high temperature bcc β-Zr value. This indicates that upon initial transformation, the bcc Zr/bcc Nb interface is semicoherent. Upon further reduction in the Zr layer thickness, the bcc Zr layer has been shown to become coherent with Nb.[8] The formation of β-Zr instead of a coherent bcc Zr phase with Nb suggests negligible coherency strains in stabilizing the bcc pseudomorph. Thus, a linear boundary can be drawn separating the two phase fields.[7] The presence of a coherently stabilized bcc Zr phase with its subsequent elastic strain energy contributions has been modeled with an appropriate curved coherency boundary and can be found elsewhere.[8]

TABLE II. The measured lattice constants from XRD and TEM.

Phase in multilayer	Lattice parameter (Å)	Specimen location on biphase diagram
α-Ti	$a = 2.95$ $c = 4.68$	Ti/Nb #5
β-Ti	$a = 3.30$	Ti/Nb #6
α-Zr	$a = 3.21$ $c = 5.10$	Zr/Nb #1
β-Zr	$a = 3.54$	Zr/Nb #2
Coherent bcc Zr	$a = 3.38$	Zr/Nb #3
bcc Nb	$a = 3.30$	Zr/Nb #1

The corresponding specimen location on the biphase diagram is listed for reference.

The slope of the biphase boundary between hcp Zr/bcc Nb and bcc β-Zr/bcc Nb was used to estimate experimentally the interfacial free energy reduction upon a change in phase stability [Eq. (2)]. This value is listed in Table I. The measured lattice values for the different phases identified in this system are compiled in Table II.

For a first approximation in determining which layer thicknesses and volume fractions could stabilize bcc Ti in Ti/Nb multilayers, a proposed biphase stability boundary, shown in Fig. 3(a) as a dotted line, was plotted using the same interfacial free energy reduction measured in the case of Zr/Nb.[8] Obviously, Zr and Ti would contribute a different chemical and structural component to the respective Zr/Nb and Ti/Nb interfaces, but this first approximation in $\Delta\gamma$ allows an initial boundary as an experimental starting point for exploring regions of possible bcc Ti stabilization. The solid line in Fig. 3(a) shows the experimentally determined hcp/bcc–bcc/bcc biphase boundary for the Ti/Nb system. The RXRD scan in Fig. 3(b) of the Ti/Nb #5 multilayer in Fig. 3(a) diffracts both the {0002} Ti peak and the {011} Nb textured peaks. Plan-view TEM diffraction in Fig. 3(c) confirms the bulk equilibrium phases. Similar to Zr in Zr/Nb, upon a reduction in layer thickness for a similar volume fraction of Nb, the Ti layer undergoes an allotropic phase transformation from hcp to bcc. As compared to Fig. 3(b), the RXRD pattern in Fig. 3(d) of the Ti/Nb #6 multilayer does not diffract the {0002} hcp intensity but a single {011} peak. The TXRD pattern in Fig. 3(e) confirms this change in phase stability. Recall that the incident x-ray radiation is different between the RXRD and TXRD experiments, thus the angular scales correspond to that difference, but the d-spacing of the {011} peak is equivalent. The absence of the hcp Ti's {10$\bar{1}$0} intensity in the TXRD pattern of Fig. 3(e) is marked to indicate that a change in bcc phase stability has resulted. Additional confirmation of bcc Ti/bcc Nb can be seen in the plan-view electron diffraction pattern of Fig. 3(f). Similar to the bcc Zr, the bcc Ti layers, upon transformation, adopted a lattice parameter similar to its high-temperature bcc β-Ti value. Unlike β-Zr, the high-temperature β-Ti phase's lattice parameter is less than 1% different than Nb.[14] This allows the bcc Ti layers to

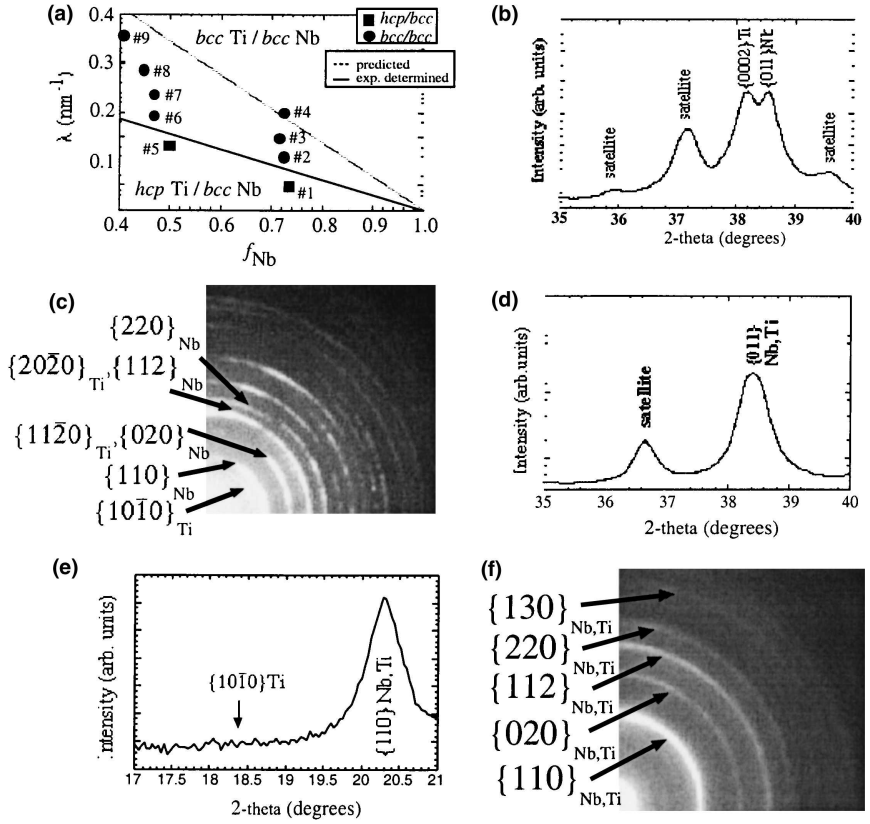

FIG. 3. (a) Biphase stability diagram for the Ti/Nb multilayers as a function of volume fraction and bilayer thickness. The dotted line is the predicted boundary whereas the solid line is the experimentally determined boundary. (b) Reflection XRD geometry pattern of the Ti/Nb #5 multilayer. Diffraction indicates the textured growth of the closest-packed-planes for both the hcp and bcc phases in the multilayer. (c) TEM plan-view diffraction pattern of the Ti/Nb #5 multilayer. The pattern was consistently indexed to the hcp Ti and bcc Nb phases. (d) Reflection XRD geometry pattern for the Ti/Nb #6 multilayer. The textured growth diffracts a single bcc {011} intensity. (e) Transmission XRD pattern of the Ti/Nb #6 multilayer. The diffraction pattern confirms the absence of the hcp Ti phase to a single bcc phase. The absent location of the hcp {10$\bar{1}$0} reflection is marked. (f) TEM plan-view diffraction pattern of the Ti/Nb #6 multilayer. The pattern was consistently indexed to a single set of bcc reflections in agreement with the XRD results.

maintain a coherent interface with the bcc Nb layers with negligible coherency strains, as confirmed from the experimentally determined linear fitted boundary in Fig. 3(a). Therefore, the thermodynamic framework description of volumetric and interfacial energy can be used without the addition of the strain energy component, and the strain-free ΔG_{Ti}, listed in Table I, can be applied directly to Eq. (2) in estimating the interfacial free energy reduction. The change in interfacial free energy accompanying the hcp–bcc transformation in the Ti layers, determined from the experimental slope of the biphase boundary in Fig. 3(a), is listed in Table I. The lattice parameters for the different phases in the Zr/Nb and Ti/Nb multilayers are listed in Table II.

The texturing pattern of the plan-view TEM diffraction patterns for Zr/Nb[8] and the Ti/Nb multilayers indicated that the hcp/bcc interface has a Burgers or near Burgers orientation relationship given as

$$(0001)\ \text{hcp} \,//\, (011)\ \text{bcc}$$
$$\langle 11\text{~}\bar{2}0\rangle\ \text{hcp} \,//\, \langle 111\rangle\ \text{bcc} \quad .$$

Upon transformation to a bcc/bcc interface, the orientation relationship is

$$(011)\ \text{bcc} \,//\, (011)\ \text{bcc}$$
$$\langle 111\rangle\ \text{bcc} \,//\, \langle 111\rangle\ \text{bcc} \quad .$$

IV. DISCUSSION

The pseudomorphic bcc phases in the Zr and Ti layers of Zr/Nb and Ti/Nb multilayers exhibited certain similar characteristics. In both cases, on reduction of the bilayer thickness, the pseudomorphic bcc phase initially adopts a lattice parameter of either Zr's or Ti's respective high-temperature β phase suggesting negligible coherency strains. This indicates the change in phase stability is not a strain-driven transformation but rather an interfacial free energy reduction from a change in the misfit dislocation network and/or chemical bonding across the interface with respect to the bulk equilibrium phase in stabilizing the pseudomorphic bcc phase. In the case of

Zr/Nb multilayers, a semicoherent, not a coherent, interface developed. Only upon a further reduction in bilayer thickness does the Zr/Nb interface become fully coherent.[8]

While there are similarities between the transformations in the two systems, there is a clear difference in the critical transformation layer thicknesses for hcp–bcc transformation. A biphase diagram depicting the hcp/bcc–bcc/bcc biphase stability boundaries for both the Zr/Nb and Ti/Nb systems is shown in Fig. 4. The solid line is the biphase boundary for the Zr/Nb multilayers, whereas the dotted line is the biphase boundary for the Ti/Nb multilayers. It is evident from the positions of these two boundaries that the critical transformation thickness for the Ti layers is substantially larger than that for the Zr layers. This fact is reflected in the substantially larger value of $\Delta\gamma$ in case of Ti/Nb as compared with Zr/Nb (Table I).

Using the orientation relationships given above and the lattice parameters shown in Table II, the misfit for the hcp/bcc and bcc/bcc interfaces was determined along the "best-fit" direction (e.g., the $\langle 11\bar{2}0\rangle//\langle 111\rangle$ and $\langle 111\rangle//\langle 111\rangle$, respectively). The Zr/Nb interface misfit is reduced from 12% to 7% upon the change from hcp to bcc Zr (for the semicoherent interfaces). Ti/Nb exhibits a reduction from 3% to 0% (coherent interface) upon the initial change in phase stability. The relative misfit reduction from an hcp/bcc to a *bcc/bcc* interface is slightly greater for Zr/Nb than for Ti/Nb.

A van der Merwe interfacial energy model for two semi-infinite layers contacted at a single interface has been used to estimate the change in interfacial free energy as a function of misfit.[17,18] The total interfacial free energy, E, is given as a linear combination of the potential energy, E_p, and the strain energy, E_s, by the following

$$E = E_p + E_s\,(\mu_I c^2/4\pi^2 d)\{1 + \beta - (1 + \beta^2)^{1/2} - \beta\,\ln[2\,\beta\,(1 + \beta^2)^{1/2} - 2\,\beta^2]\} \quad , \tag{3}$$

where μ_I is the interfacial shear modulus (taken to be the average of the two constituent phases), c is a spacing parameter formed by the superposition of the two lattices in contact at the interface, d is the distance between the two atomic planes on either side of the interface, and β is a function that contains all the significant contributions to the interfacial free energy such as the misfit and the elastic constants of the crystals. The β function is given as

$$\beta = 2\pi d\Lambda/\mu_1 p \quad , \tag{4}$$

with d and μ_I defined above, Λ is

$$\Lambda = \{[(1 - \nu_A)/\mu_A] + [(1 - \nu_B)/\mu_B]\}^{-1} \quad . \tag{5}$$

where ν_i and μ_i is Poisson's ratio and the shear modulus of layer i, and the ratio of d/p in Eq. (4) is

$$d/p = (a - b)/[1/2(a + b)] \quad ,$$

where a and b are the respective crystallographic lattice parameters at the interface determined by the orientation relationship. The ratio of d/p is a measure of the misfit dislocation spacing, which is assumed in this model to be a series of parallel dislocations at the interface. The elastic constants used in the calculations for the above equations are given in Table III.

The calculated change in interfacial energy as a function of β for the hcp/bcc and bcc/bcc interfaces in Zr/Nb and Ti/Nb systems, respectively, are plotted in Figs. 5(a) and 5(b). The arrows mark the experimentally determined value of β for each multilayer in its respective phase stability condition and misfit at the interface. The difference in the interfacial free energy of each state at their respective β value is then the calculated estimate of the $\Delta\gamma$. The plots in Fig. 5 exhibit how interfacial energy scales with β. As β increases, or alternatively as misfit is increased, the interfacial free energy increases. The greatest increase in interfacial energy occurs with the initial insertion of misfit dislocations (low β values). This trend explains why Ti would have a greater driving force for the hcp–bcc transformation. When Ti undergoes a phase stability change from hcp to bcc, it is able to

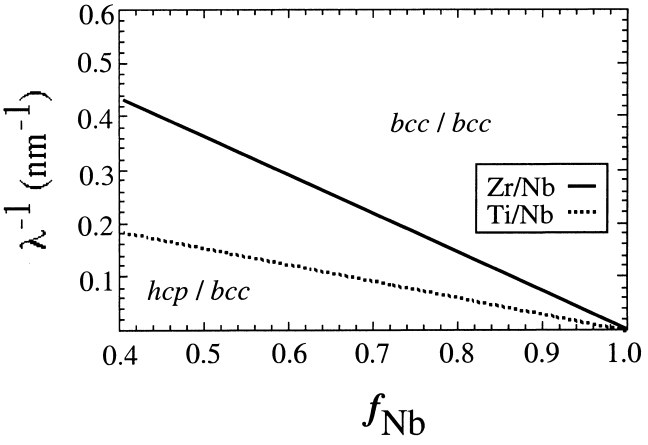

FIG. 4. A combined biphase stability diagram for the Zr/Nb and Ti/Nb multilayer systems. The solid line represents the phase stability boundary for Zr/Nb, and the dashed line represents the phase stability boundary for Ti/Nb. The plot clearly indicates that the Ti layers experience a change in phase stability at a much larger layer thickness than that of Zr for a similar volume fraction of Nb.

TABLE III. The elastic constants of the phases used in determining the change in interfacial free energy with misfit for the van der Merwe interfacial energy model.

Phase	ν	μ (GPa)	Reference
α-Zr	0.38	35	14
α-Ti	0.361	45.6	14
β-Zr	0.39	27.1	19
β-Ti	0.372	33	19
Nb	0.397	37.5	14

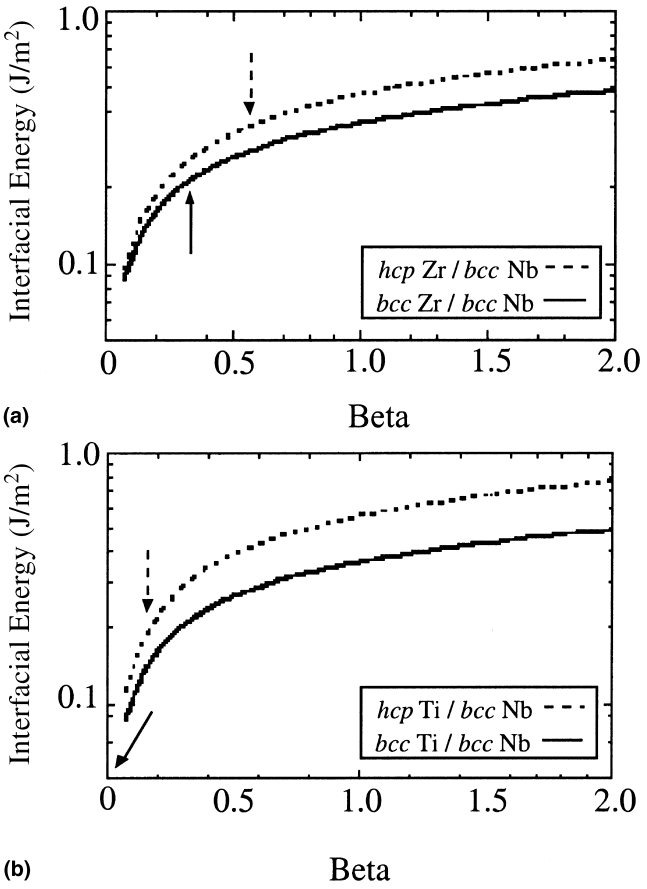

FIG. 5. (a) A van der Merwe interfacial energy plot for the hcp/bcc and bcc/bcc interfaces for the Zr/Nb multilayers. The arrows indicate the location of the experimentally determined β values for the multilayers. Note that the interfacial free energy rises rapidly with initial increase in values of β. (b) A van der Merwe interfacial energy plot for the hcp/bcc and bcc/bcc interfaces for Ti/Nb multilayers. Even though Zr/Nb has a larger reduction in misfit with change in phase stability, the Ti/Nb multilayer, clearly indicated by this plot, has a significant reduction in interfacial free energy by the formation of the coherent interface.

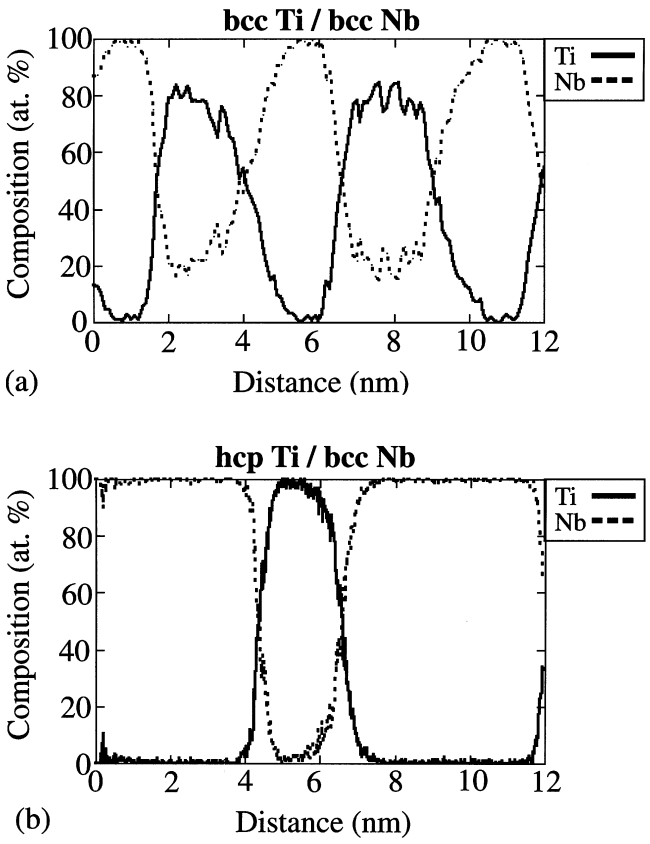

FIG. 6. (a) Compositional profile of a bcc Ti/bcc Nb multilayer characterized by atom probe tomography. Substantial interdiffusion of Nb into the Ti layers has facilitated the bcc Ti phase stability to a much larger layer thickness. (b) Compositional profile of an hcp Ti/bcc Nb multilayer characterized by atom probe tomography. Unlike the bcc Ti phase, negligible Nb interdiffusion has occurred in the hcp layers.

reduce significantly its interfacial energy by the formation of a coherent interface or, alternatively, the structural component of interfacial energy is reduced to zero. Though Zr has a greater overall reduction in misfit upon a change in phase stability, it is unable to reduce the structural component of its interfacial energy to zero because it has formed a semicoherent interface with Nb.[8] The calculated interfacial free energy difference using this simple model for the Ti/Nb multilayer is approximately –280 mJ/m^2 as compared to Zr/Nb's interfacial free energy difference of –240 mJ/m^2.

As listed in Table I, reasonable agreement was observed between the $\Delta\gamma$ values calculated from the van der Merwe model and the experimental value for Zr/Nb. However, such a close agreement was not observed in case of the Ti/Nb. Because each system is subjected to the same simple assumptions of the van der Merwe model, additional contributions may be influencing the free energy contributions to Ti/Nb.

The compositional profile characterized by APT for a bcc Ti/bcc Nb multilayer and a hcp Ti/bcc Nb multilayer is shown in Fig. 6. It is clear from Fig. 6(a) that Nb has significantly interdiffused into the bcc Ti layers to a concentration of approximately 20 at.%. Niobium, being a bcc-stabilizer in Ti alloys and having significantly interdiffused into the Ti layer, will have a marked influence on the free energy values of the system. Based on the APT compositional results, the equilibrium volumetric free energy difference, ΔG_{Ti}, between bcc and hcp Ti has been refined to include the Nb concentration. Using the refined $\Delta G_{Ti\text{-}20Nb}$ value, listed in Table I, and the experimental slope of the biphase stability boundary in Fig. 3(a), the $\Delta\gamma$ was recalculated to be approximately –283 mJ/m^2. This value is much closer in agreement with the predictions afforded by the van der Merwe model. In contrast to Fig. 6(a), the compositional profile of an hcp Ti/bcc Nb multilayer shown in Fig. 6(b) has negligible Nb interdiffusion in the hcp Ti layer.

The substantial Nb interdiffusion in the bcc Ti layers is quite surprising, particularly as the film was grown at ambient temperatures in which diffusion should be limited. One of the potential factors that could be contributing toward the enhanced interdiffusion of Nb into the bcc Ti layers is the similar atomic radius of Ti (0.0955 nm) and Nb (0.0953 nm).[14] In contrast, the atomic radius of Nb differs significantly from that of Zr (0.104 nm).[14] The authors have recently reported Meissner effect measurements of the superconducting critical transition temperature, T_c, for Zr/Nb multilayers.[20] The value of T_c for these multilayers is strongly influenced by the degree of intermixing between the layers.[4] However, because the experimentally measured T_c values could be rationalized using a proximity effect model for multilayers with abrupt interfaces, it appears that there is negligible intermixing in case of the Zr/Nb multilayers.[20] The good agreement of the predicted value of $\Delta\gamma$ based on the van der Merwe model with the experimental value for the Zr/Nb multilayers also suggests negligible intermixing in the Zr/Nb system. Attempts to characterize a Zr/Nb atom probe specimen tip have proven unsuccessful to date.

It is still unclear and the focus of current work[21] by the authors to understand the driving force for this substantial interdiffusion phenomenon, particularly when the Nb concentration is substantially greater in the bcc Ti versus the hcp Ti layers. The results of this interdiffusion, coupled to the first approximation modeling of the interfacial energy, demonstrate the significant factor chemical compositions have in stabilizing pseudomorphic phases beyond coherency strains and interfacial free energy reduction.

V. CONCLUSIONS

A comparison of the hcp–bcc transformations in Zr and Ti layers in Zr/Nb and Ti/Nb multilayers has been reported in this paper. The studies have been conducted on a series of sputter-deposited Zr/Nb and Ti/Nb multilayers with varying bilayer thicknesses and volume fractions of Nb. For Nb-rich volume fractions, the Zr and Ti layers undergo a change in phase stability from hcp to bcc with a reduction in bilayer thickness. This has been attributed to a reduction in the interfacial free energy rather than a coherency strain driven transformation. The critical transformation thickness for the hcp–bcc transformation in the Ti layers in Ti/Nb is substantially larger than that of the Zr layers in the Zr/Nb multilayers. Atom probe results of the Ti/Nb multilayers have indicated that Nb has significantly interdiffused into the Ti layer helping to facilitate its hcp to bcc phase stability. A simple van der Merwe interfacial energy model has also indicated that the interfacial free energy reduction is greater for a change in phase stability in the Ti/Nb than the Zr/Nb multilayers. The van der Merwe model provided an estimated benchmark of the expected interfacial free energies. The atom probe's compositional profile of Ti/Nb allowed the associated volumetric free energies of this system to be refined in the thermodynamic model resulting in much closer agreement of the estimated experimental and calculated interfacial free energy reduction values.

ACKNOWLEDGMENTS

The authors thank Mr. Arda Genc for the preparation of the cross-section sample shown in this paper and Dr. Paul Zschack for help in the experimental set-up of the transmission x-ray diffraction experiments at the Advanced Photon Source. This work was funded by the Center for the Accelerated Maturation of Materials (CAMM) at The Ohio State University. The UNICAT facility at the Advanced Photon Source (APS) is supported by the University of Illinois at Urbana-Champaign, Materials Research Laboratory (U.S. Department of Energy, the State of Illinois-IBHE-HECA, and the NSF), the Oak Ridge National Laboratory (U.S. Department of Energy under contract with UT-Battelle, LLC), the National Institute of Standards and Technology (U.S. Department of Commerce), and UOP LLC. The APS is supported by the U.S. Department of Energy, Basic Energy Sciences, Office of Science under Contract No. W-31-109-ENG-38. Atom probe research at the Oak Ridge National Laboratory SHaRE Collaborative Research Center was sponsored by the Division of Materials Sciences and Engineering, U.S. Department of Energy, under Contract No. DE-AC05-00OR22725 with UT-Battelle, LLC.

REFERENCES

1. R. Clarke, F. Lamelas, C. Uher, C.P. Flynn, and J.E. Cunningham, *Phys. Rev. B* **34,** 2022 (1986).
2. H. Wormeester, E. Huger, and E. Bauer, *Phys. Rev. Lett.* **77,** 1540 (1996).
3. G.A. Prinz, *Phys. Rev. Lett.* **54,** 1051 (1985).
4. W.P. Lowe and T.H. Geballe, *Phys. Rev. B* **29,** 4961 (1984).
5. N. Metoki, W. Donner, and H. Zabel, *Phys. Rev. B* **49,** 17351 (1994).
6. R. Banerjee, S.A. Dregia, and H.L. Fraser, *Acta Mater.* **47,** 4225 (1999).
7. S.A. Dregia, R. Banerjee, and H.L. Fraser, *Scr. Mater.* **39,** 217 (1998).
8. G.B. Thompson, R. Banerjee, S.A. Dregia, and H.L. Fraser, *Acta Mater.* **51,** 5285 (2003).
9. A.I. Guillermet, *Zeitshrift fur Metallkunde* **82,** 478 (1991).
10. L. Kaufman and H. Nesor, Calphad **2,** 81 (1978).
11. J. Bonevich, D. van Heerden, and D. Josell, *J. Mater. Res.* **14,** 1977 (1999).
12. R. Banerjee, S.A. Dregia, and H.L. Fraser, *Acta Mater.* **47,** 4225 (1999).
13. J.Q. Zheng, J.B. Ketterson, C.M. Falco, and I.K. Schuller, *Physica* **108B,** 290 (1981).

14. *Smithells Metals Handbook*, 7th ed., edited by E.A. Brandes and G.B. Brook (Butterworth and Heinemann Ltd., London, U.K. 1992).
15. D.J. Larson, B.D. Wissman, R.J. Viellieux, RL. Martens, T.T. Gribb, H.F. Erskine, T.F. Kelly, and N. Tabat, *Microscopy and Microanalysis.* **7,** 24 (2001).
16. G.B. Thompson, H.L. Fraser, and M.K. Miller, Ultramicroscopy (2004, in press).
17. J.H. van der Merwe, *J. Appl. Phys.* **34,** 117 (1963).
18. J.H. van der Merwe, Proceedings of the Physical Society of London, Sec. A **63,** 616 (1950).
19. Q. Chen and B. Sundman, *Acta Mater.* **49,** 947 (2001).
20. R. Banerjee, P. Vasa, G.B. Thompson, P. Ayyub, and H.L. Fraser, *Solid State Commun.* **127,** 349 (2003).
21. G.B. Thompson, M.K. Miller, R. Banerjee, and H.L. Fraser, in *Continuous Nanophase and Nanostructured Materials*, edited by S. Komarneni, J.C. Parker, and J. Watkins (Mater. Res. Soc. Symp. Proc. **788,** Warrendale, PA, 2003), p. L2.8.1.